Analysis of current collection in a tubular SOFC

Hodjati-Pugh, Oujen; Andrews, James; Dhir, Aman; Steinberger-Wilckens, Robert

DOI:
10.1016/j.jpowsour.2021.229780

Document Version
Peer reviewed version

Citation for published version (Harvard):
Hodjati-Pugh, O, Andrews, J, Dhir, A & Steinberger-Wilckens, R 2021, 'Analysis of current collection in a tubular SOFC: an empirical and mathematical modelling approach for minimised ohmic polarisation', *Journal of Power Sources*, vol. 494, 229780. https://doi.org/10.1016/j.jpowsour.2021.229780

Analysis of current collection in micro-tubular solid oxide fuel cells: An empirical and mathematical modelling approach for minimised ohmic polarisation

O. Hodjati-Pugh[a], J.Andrews[b], A. Dhir[c], R. Steinberger-Wilckens[a]

[a]Centre for Fuel Cell and Hydrogen Research,

School of Chemical Engineering, University of Birmingham, B15 2TT

[b]School of Mathematics, University of Birmingham, B15 2TT

[c]School of Chemical Engineering, University of Wolverhampton, WV1 1LY

ABSTRACT

Data from electrochemical impedance spectroscopy (EIS) of a 152 mm long, 6.8 mm outer diameter (OD) segmented-in-series micro-tubular solid oxide fuel cell (μT-SOFC) coupled with equivalent circuit modelling (ECM) support a circuit model and a continuum resistance path model to investigate the ohmic polarisation and current distribution for various current collector configurations on a micro-tube. Minimising the characteristically long axial current conduction pathways of μT-SOFCs is critical to maximise cell performance, particularly of cells more than a few centimetres long. Optimal positioning of a single current collector minimises the performance losses from the electrode. Multiple current collector terminals increase cell performance over a single terminal, but positioning must still be optimised. Sizing of the current collector terminal is critical to limit the loss of active area of the cathode. A trade-off between terminal sizing/spacing

and loss of active area can lead to sub-optimal current collection. The models are generalised for all possible current collector configurations. We identify simple criteria to determine the maximum current collection efficiency of single and multiple anode current collectors for a range of cell geometries. The design tool allows early consideration to cell sizing as a function of anode current collection during cell and stack development.

Keywords: Tubular SOFC, segmented cell, current collection, numerical analysis, ohmic polarisation, impedance, circuit model, resistance path model, continuum model

1. Introduction

Fuel cells are a promising technology for the efficient conversion of chemical energy into electrical energy, exhibiting a typical electrical efficiency of up to and above 60 % [1,2]. Provided the fuel cell is fed with 'green hydrogen' (from water electrolysis with renewable energy sourced electricity) or biogas, fuel cells are a 'zero-emission' technology that can play a pivotal role in a move away from fossil fuels. The scalable nature of fuel cells allows them to produce power over a wide range, from the order of a few mW to 100's of MWs, enabling them to compete with incumbent technologies in the transport, energy and industrial sectors to name but a few [3]. High-temperature fuel cells, such as the solid oxide fuel cell (SOFC) produce power and high-quality heat and power (CHP) efficiency in the range of 85-95 % [4].

The development of micro-tubular SOFC (μT-SOFC) technology is not as mature as that of planar variants, however, the micro-tubular cell has several advantages over a planar cell, namely facile sealing and manifolding, high thermal cycling tolerability, rapid start-up times and high mechanical durability [4,5,6]. The advantages, in addition to the excellent power density by mass and volume of μT-SOFC stacks lend them to portable power generation, a domain not typically accessible for planar SOFCs [7,8,9].

A key area for development of μT-SOFC is current collection. Regardless of support configuration (cell designs include anode, electrolyte or cathode supported cells), the current conduction pathways

are significantly longer in tubular versus planar geometries [11,12]. Minimisation of conduction pathways and hence the minimisation of the ohmic polarisation contribution is therefore key to maximise cell performance. High ohmic resistances, particularly along the cell length (in the axial dimension) can restrict cell design and inhibit optimisation concerning cell size and cost [13,14]. Understanding the current distribution in μT-SOFCs is therefore crucial for optimised current collector design, leading to improved manufacturing procedures and ultimately maximised performance.

The understanding of the ohmic resistance and its effect on current distribution can be approached by using empirical and numerical methods. The former can be costly and time-consuming yet provides real-world information from electrochemical data such as polarisation curves and electrochemical impedance spectroscopy (EIS), as well as from conductivity testing and material characterisation. An empirical study for optimising anode current collection was conducted by Bai et al. [15] on a single chamber segmented tubular cell 4.8 cm in length with an outer diameter (OD) of 7 mm. They concluded that an increase in the number of current collection points from 1 to 5 increased the maximum power density. However, they did not explore the positioning of the single terminals and only looked at five of the possible 31 configurations. Contrary to this research, Meadowcroft et al. [16] found that a 152 mm long cell with 6.7 mm OD with a single current collection node at the centre of the cathode was superior to that of a cell with current collection at either end of the active region (cathode length).

Suzuki et al. developed a circuit analysis to determine current collection efficiency for their 1.6 mm OD micro-tubular cell [17]. However, they were unable to determine the exact analytical solution to the model but did establish that an analytical solution should exist. Furthermore, they only considered current collectors located at the start and/or end of the μT-SOFC active area. They also published research for their smaller 0.8 mm OD cell to estimate the limit of using one end current terminal as a function of anode tube length and thickness [18].

In this study, we focus on developing models of the ohmic polarisation and its effect on cell

performance. A circuit analysis model is presented that encompasses the two circuits considered by Suzuki et al. [17,18] but extends their results in three ways. Firstly, the positions of the current collectors do not need to be at the start or end of the μT-SOFC active area but can be located anywhere along the length of the μT-SOFC tube. Secondly, exact analytical solutions are obtained and thirdly, the number of current collectors can be arbitrary. A second resistance path model is obtained starting from path length arguments. It will be shown that the circuit analysis and resistance path method are equivalent. A current collection strategy specifies the locations of the current collectors given the size of the terminals. The optimal strategy determines the number of current collectors for a given length to maximise the current density and depends on different definitions of the current density.

The model will use empirically derived electrochemical data from state-of-the-art tubular cells (6.8 mm OD, 20 cm^2 active area) for fitting. Polarisation data from two configurations of segmented micro-tubular cells with either three or five current collection nodes along with EIS data give key insight into the global polarisation resistances from activation, mass transport and ohmic losses. EIS data is particularly useful for extracting information on ohmic losses from different current collection position configurations. The model will serve as a predictive tool for the cell manufacturer to make decisions on cell design from the perspective of minimisation of area specific resistance (ASR), thus improving overall cell performance.

2. Empirical Approach

2.1 Cell specification

The micro-tubular SOFC cells used for this study were complete, state-of-the-art cells previously detailed in 2019 [19]. The anode supported cell had an outer diameter of 6.8 mm and a total cell length of 152 mm as seen in the supporting material (Supporting Material (SM) Fig 22. The YSZ electrolyte covered the entirety of the cell length while the LSCF cathode covered 95.5 mm, giving an available active area of approximately 20 cm^2. A layer of GDC acted as a barrier layer between the electrolyte and LSCF cathode. The anode was

approximately 560 μm in thickness, the electrolyte 10 μm, the barrier layer 8 μm and the cathode 55 μm.

2.2 Cell segmentation and current collection

To obtain an understanding of the current distribution of the cell when collecting at different current collector positions, the cell was segmented according to two designs. The first had three equidistant anode terminals symmetrically arranged around the centre of the active region. The second had five equidistant anode terminals, again symmetrically arranged around a current collecting node in the centre of the active region (cathode). The nodes of the three-terminal and five-terminal designs were all within the active region of the cell. The former resulting in two cathode segments of equal length, and the latter in four cathode segments of equal length.

The segmentation was achieved by removal of 8 mm rings of cathode, barrier layer and electrolyte to expose the anode support from the cell exterior. The cathode and barrier layer were removed by a fine blade while the electrolyte was polished away using a fine 150 grit file. A dense silver paste was applied to the exposed anode terminals before attaching braided silver wires. The cathode segments were painted with a porous silver paste and wired in a stripe-and-band configuration, similar to the style of Meadowcroft et al. [16]. Each cathode wire was connected in-series to a common rail. Silver voltage sensing wires were added in a four-probe measurement configuration. The prepared cell and geometry is seen in Fig. 1a. Ceramic fuel inlet and outlet manifolds were attached to the cell using Ceramabond ceramic sealant [20]. Manifold joints and anode current collector joins were sealed with glass-sealant [21].

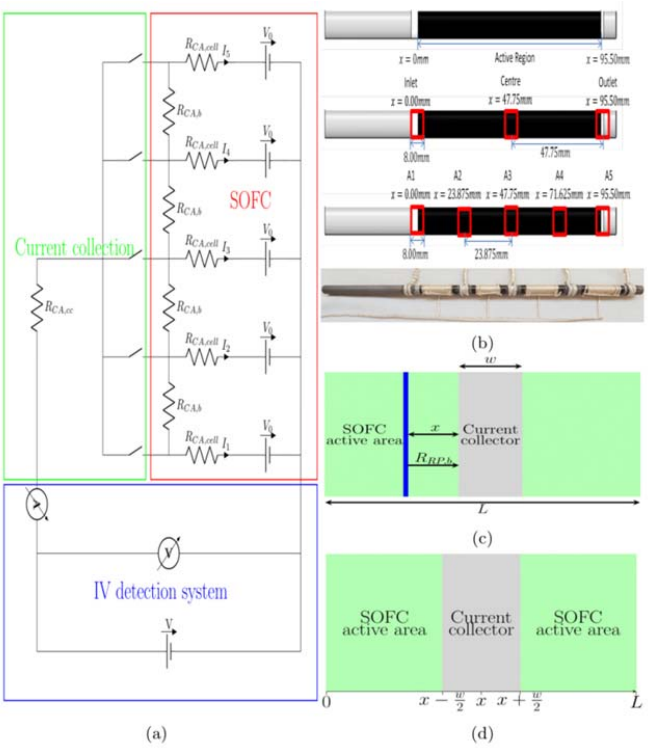

Figure 1: (a) Schematic circuit representation of the 5 current collector terminal segmented µT-SOFC (b) segmented µT-SOFC geometry with 3 and 5 current collector terminals and 5 terminal cell ready for testing, (c) schematic for the resistance path model; green represents the µT-SOFC and the blue stripe represents a ring element of infinitesimal thickness, (d) geometry for a single current collector case.

2.3 Electrochemical testing

Experiments were conducted at 750°C using an Elite Thermal Systems horizontal furnace. Electrochemical performance was evaluated with a Solartron Analytical 1470E unit coupled to a 50 V/25 A booster and Solartron Electrochemical Impedance Spectroscopy (EIS) unit. The electrochemical testing profile was controlled and obtained with a data logger running Cell Test software. The cell was fed with dry hydrogen during start-up (from 400°C) and tested at a hydrogen flow rate of 200 ml.min^{-1}. The flow was sufficiently high to ensure the fuel was in excess at peak current density, avoiding starvation and mass transport losses, these effects not being at the focus of this study. Oxygen was supplied from the air chamber inside the furnace, assumed to be at the furnace temperature. The oxygen was assumed to be in excess and circulated by natural diffusion. Impedance measurements were recorded between a frequency of 0.1 and 1x10^{6} Hz with a perturbation amplitude of 10 mV. Measurements were made at 0.7 V, safely sitting in the ohmic loss dominated region of the i-V-curve.

3. Modelling Approach

3.1 Configurations

Two models were developed to represent three and five current collector terminals. A circuit model approach represented the system as five connected voltage elements within a resistance network. Fig. 1b provides a schematic of the electrochemical circuit and the measurement circuit. A resistance path model was also developed, enabling greater accounting for the current generation.

The switches in Fig. 1a were to be set 'on' or 'off' to create 2^5=32 different circuit configurations. A binary representation of the switches in Fig. 1b is '00000', where all the switches are in the 'off' position. The i^{th} switch is in line with the i^{th} resistor, and the binary representation is a 1/0 in the i^{th} position, depending on the switch state. All 31 complete circuits were considered, i.e. 00000 was not included. This binary representation was also used to indicate the multiple connections for the resistance path models. For the 5 terminal segmented-in-series μT-SOFC setup, a cell extracting current through a single 'on' current collector terminal located at the inlet, centre or outlet would have binary representation of 10000, 00100 and 00001, respectively. Similarly, for the 3 terminal segmented-in-series μT-SOFC setup, a cell extracting current through a single current collector terminal located at the inlet, centre or outlet would have binary representation of 100, 010 and 001, respectively. Extending the terminology to the 3 terminal segmented-in-series μT-SOFC cell extracting current through multiple current collector terminals: 101 represents current extracted through the inlet and outlet terminals, 110 represents current extracted through the inlet and central terminals, 011 represents current extracted through the central and outlet terminals, 111 represents current extracted through the inlet, central and outlet terminals.

3.2 Circuit model

μT-SOFCs have overall resistances that depend on the length of the fuel cell and on the internal resistance. For μT-SOFC these resistances are a resistance radially across the μT-SOFC, $R_{CA,\text{cell}}$, and longitudinally along the tube, $R_{CA,\text{b}}$. The μT-SOFC is

represented by an equivalent circuit that depends on these two parameters and any additional ohmic resistance. The combined ohmic resistance from the μT-SOFC and the resistance from the current collector is the current collector resistance, $R_{CA,\mathrm{cc}}$.

The following assumptions are required for the circuit analysis:

1) It is assumed that an approximate resistance and cell circuit model can be constructed as in Fig. 1 (a)
2) Kirchhoff's current law is valid.
3) Kirchhoff's voltage law is valid.
4) For the results presented in the manuscript, the potential difference generated by the chemical reaction is assumed to be independent of location along the active region.

Condition 4) can be relaxed, allowing the variation of the chemical reactions due to temperature and fuel composition to be considered. The supporting material (SM §2.3.4) details the general case given by Eqn. 32 without this assumption. In the research published by Suzuki et al. [17,18] additional parallel paths are added between the μT-SOFC connections to better approximate the circuit, and they present approximate solutions for the cases of 100, 001 and 101. They did not present the exact analytical solutions as $n\to\infty$, the derivation of which can be found in SM §2.3.4 and 2.3.6. The total resistance from the circuit analysis for the two configuration 100 and 101 are given by:

$$R_{\mathrm{TCA},100}=R_{\mathrm{TCA},001}=R_{CA,\mathrm{cc}}+A \tag{1}$$

$$R_{\mathrm{TCA},101}=R_{CA,\mathrm{cc}}+A/2, \tag{2}$$

respectively. In general $R_{\mathrm{TCA,con}}$is the total resistance of the μT-SOFC for the configuration given by config. The circuit analysis as $n\to\infty$ reveals A:

$$A=(\sqrt{(1+4R_{CA,\mathrm{cell}}/R_{CA,\mathrm{b}})}-1)R_{CA,\mathrm{b}}/2. \tag{3}$$

$R_{CA,\mathrm{cell}}$ is envisioned as the resistance radially across the fuel cell and $R_{CA,\mathrm{b}}$ as the resistance along the μT-SOFC as depicted in Fig. 1b. To complete the set of basic configurations from which all other

configurations may be constructed 010 is (SM §2.3.5):

$$R_{\mathrm{TCA},010} = R_{CA,\mathrm{cc}} + A/2. \quad (4)$$

All configurations take the form:

$$R_{\mathrm{TCA,config}} = R_{CA,\mathrm{cc}} + A/K_{\mathrm{config}}, \quad (5)$$

where K_{config} is a coefficient depending on the configurations labelled as config (SM §2.3.7 and 2.3.8). The circuit analysis approach detailed in the supporting material allows K_{config} to be determined analytically for all possible configurations, a list of typical values may be found in (SM Table 2).

3.3 Resistance path model

This model allows for current-generation along the entire length of the μT-SOFC. Treating the resistance along the μT-SOFC, $R_{\mathrm{RP,b}} = r\langle l \rangle$ where r is the resistance per unit length and $\langle l \rangle$ is the average path length of a μT-SOFC ring to the current collector as represented in Fig. 1d. Placing one current collector at one end of the μT-SOFC, the average path length is, $\langle l \rangle = L/2$, where L is the length of the μT-SOFC active area. $R_{\mathrm{RP,cell}}$ gives the resistance radially across the cell. Ignoring the resistance of the current collector itself, the resistance path model allows the current generated per infinitesimal length of the ring element to be given by:

$$\hat{\imath} = -(V_0 - V) r / (R_{\mathrm{RP,cell}} + rx)^2 \quad (6)$$

where x is the distance from the ring to the nearest current collector (SM §3.1.3). Further, V_0 is the μT-SOFC potential and V is the applied potential. Eqn. (6) is used to determine the effective resistance from direct integration. Including the current collector resistance, $R_{\mathrm{RP,cc}}$, the equivalent resistance (SM §3.1.3) for the resistance path model when one current collector is placed at the start or end of the μT-SOFC active area is:

$$R_{\mathrm{TRP},100} = R_{\mathrm{TR},001} = R_{\mathrm{RP,cc}} + R_{\mathrm{RP,cell}}(R_{\mathrm{RP,cell}} + rL)/(rL) \quad (7)$$

In the case of two current collectors placed at either end of the μT-SOFC the equivalent resistance is:

$$R_{TRP,101}=R_{RP,cc}+R_{RP,cell}(R_{RP,cell}+rL/2)/(rL) \quad (8)$$

Finally, the case of a current collector placed in the middle has an equivalent resistance of:

$$R_{TRP,010}=R_{RP,cc}+R_{RP,cell}(R_{RP,cell}+rL/2)/(rL) \quad (9)$$

Similar to the circuit model any configuration can be expressed as:

$$R_{TRP,config}=R_{RP,cc}+R_{RP,cell}(R_{RP,cell}+rL/K_{config})/(rL) \quad (10)$$

where $K_{config}=L/(2\langle l\rangle)$ is a coefficient depending on the configurations labelled as 'config' (SM §3). K_{config} is calculated analytically as described in SM §3 for all possible configurations, a list of typical values may be found in (SM Table 5).

3.4 Equivalence between the two models

The two models have similar starting points, breaking down the resistances into a resistance across the μT-SOFC, along the μT-SOFC and finally, adding the current collection resistance to obtain the equivalent circuit. It might, therefore, be expected that the two models are in fact, equivalent. Should both models have the same $\underline{K}_{config}$ for every configuration, they represent the same model and $R_{CA,cc}=R_{RP,cc}+R_{RP,cell}^2/(rL)$ and $A=R_{RP,cell}$. All configurations considered throughout this work have identical K_{config} for both models (SM §2.3.7, 2.3.8, 3.5.1 and 3.5.2).

3.5 Parameter determination

There are two suggested routes to the determination of the parameters for these models, the first is EIS data, and the second is i-V-curves.

3.5.1 EIS

An equivalent RC circuit of the EIS is described by a two-time constant spectrum as shown in SM Fig. 23. The RC circuit used throughout takes an ohmic resistance and adds two elements in series consisting of a resistor in parallel with a capacitor. The three resistances from the EIS relates directly to the resistances, $\underline{R}_{\text{ohmic}}$, R_B and R_C respectively, under direct current. The EIS model can be more simply expressed as two resistor parameters instead of three by using $R_{\text{cell}}=R_B+R_C$ and $\underline{R}_{\text{ohmic}}$. The total resistance of the cell is given by, $R_{\text{ohmic}}+ R_{\text{cell}}$. Obtaining EIS data for the three configurations 100, 010 and 001 from Eqns. (1), (2), (4) and (5) for the circuit analysis model, and Eqns. (7), (8), (9) and (10) for the resistance path models, enabled the necessary parameters of the models to be determined by fitting to the circuit in SM Fig. 23 to obtain the parameters R_{ohmic}, R_B and R_C.

3.5.2 i-V-curves

While EIS data required only one set of measurements for each of the configurations at a given applied potential, *V,* the i-V-curves required more information, as the local gradient was the resistance, $R_{\text{cell}}+R_{\text{ohmic}}$, as such multiple applied potentials were required to determine this resistance. The circuit in Fig. 1c required a few voltages in the 'ohmic' region to determine the local gradient, which represents an average of the resistance (Area Specific Resistance, ASR, in the i-V-curve). From $R_{\text{cell}}+R_{\text{ohmic}}$ the three configurations, 100, 010 and 001 could be used to determine the required parameters for both models using the same set of equations as the EIS case.

4. Results and Discussion

4.1 Three current collector positions

4.1.1 EIS for parameter estimation

Typical EIS data at 0.7 V for the μT-SOFC cells may be found in Fig. 2 for the three configurations 100, 010 and 001. The equivalent circuit resistance for the three configurations were presented in Eqn. (1), (2) and (1), respectively (SM §2.3.4, 2.3.6, 2.3.7 and 2.3.8). Since the capacitance is not of interest here, only the parameter $R_{\text{ohmic}}+R_{\text{cell}}$ are presented in Table 1.

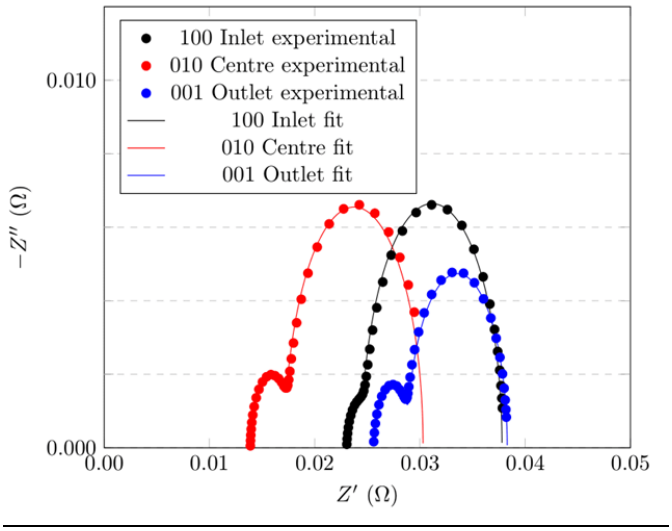

Figure 2: EIS data for three different configurations, 100, 010 and 001. Length of the active cell area is 71.5 mm.

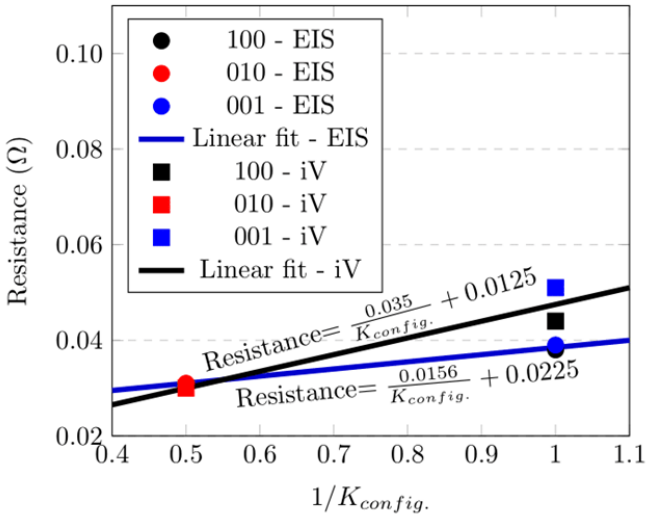

Figure 3: Resistance of the different configurations plotted against the reciprocal of $K_{config.}$ for the configuration using EIS and iV data.

To determine the key parameters of the model the resistance was plotted against the reciprocal of K_{config}, the gradient from Fig. 3 was $A=R_{RP,cell}=0.0156$ Ω and $R_{CA,cc}$ =0.0225 Ω from the resistance intercept. For the resistance path model it is not possible to determine r from only this dataset using Eqn. (10). Similarly for the circuit model, it is not possible to obtain $R_{CA,cell}$ or $R_{CA,b}$ from this data using Eqn. (3). A comparison of the experimental data and the two models in Table 1. The fit explains 99.5 % of the variation of the data; however, the data set is small due to only three configurations having been considered.

Table 1: Comparison of fitted resistance with the experimental data from EIS data.

Configuration	**Resistance path (Ω) [EIS parameters]**	**Circuit (Ω) [EIS parameters]**	**Experimental (Ω) [EIS data]**
100	0.038	0.038	0.038
010	0.030	0.030	0.031
001	0.038	0.038	0.039

4.1.2 Current-voltage data for parameter estimation

Typical i-V data for the µT-SOFC cells may be found in Fig. 4 for the same µT-SOFC cell. The gradient of the i-V curve is the area specific resistance (ASR) of the µT-SOFC and the values taken from the slope of the graph are 0.6721 Ω cm^2, 0.4519 Ω cm^2 and 0.7862 Ω cm^2 for the inlet, centre and outlet contacting position, respectively.

The analysis of the data now proceeds as with the EIS data to determine the parameters for the model.

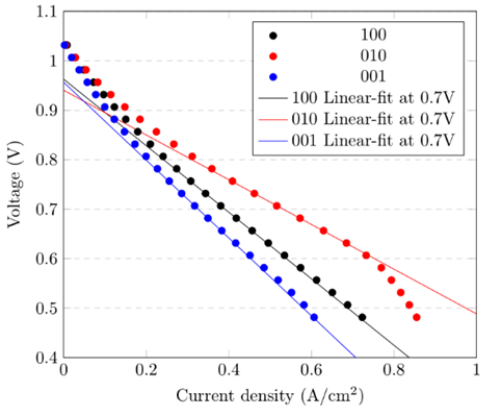

Figure 4: i-V curves for the three individual current collection connections. The gradient is obtained as a local linear equation around 0.7 V and is the ASR of the cell. The local fitting method is discussed in SM §6

Plotting the resistance against the reciprocal of K_{config}, the gradient from Fig. 3 is A=$R_{RP,cell}$=0.0350 Ω and $R_{CA,cc}$ =0.0125 Ω from the resistance intercept. The i-V data also allow for extrapolation to 0 current density (open circuit voltage, OCV) and the µT-SOFC voltage from a linear fit, shown in Table 2. The potential V_0=0.95 V is used to determine the current from I=(V_0-V)/$R_{T,config}$.

Table 2: Comparison of fitted resistance with the experimental data from i-V data.

Configuration	Resistance path (Ω) [IV parameters]	Resistance Experimental (Ω) [IV data]	Voltage Extrapolate to OCV (V) V_0
100	0.048	0.044	0.963
010	0.030	0.030	0.940
001	0.048	0.051	0.956

4.1.3 Comparison of EIS and IV parameters

The EIS data is more reliable as it determines the resistance of a µT-SOFC at a given applied voltage.

The i-V curve data supplies a single gradient value which indicates an average across the resistances at different applied voltages. The EIS resistance of the cell, or A, depending on the model, is lower by a factor of 0.67 compared with the value calculated from the i-V parameters. While the EIS resistance for the current collector is determined as 1.31 times the i-V parameter value.

Configuration 001 has a higher resistance compared to 100 in both the EIS and i-V data. This is a repeatable observation in all SOCFs. As such, a small but significant deviation from the symmetry of the models developed here is observed. There are two leading physical processes describing this decrease of current contribution from the outlet of the μT-SOFC. Firstly, changes in resistances of the μT-SOFC and current collector within the furnace due to temperature differences. Secondly, a change in μT-SOFC potential due to temperature changes and fuel depletion, according to the Nernst equation. It is therefore essential to consider the five current collector configurations and all possible permutations.

4.2 Five current collector positions

The preceding sections detailed the case of three current collectors. However, extending this to the five current collector case allows a greater variety of configurations to be considered. Only the single-current collector positions are used for parameter estimation. Then the parameters will be applied to all the configurations and averaged and compared to the experimental values.

Table 3: Comparison between resistance of the SOFC and the fitted model for each of the 5 single current collector configurations.

Configuration	**Current collector position**	**$R_{ohmic}+R_{cell}$ (Ω) [EIS data]**	**Resistance path (Ω) [EIS parameters]**
10000	**A1**	0.309	0.310
01000	**A2**	0.281	0.282
00100	**A3**	0.273	0.273
00010	**A4**	0.283	0.282
00001	**A5**	0.312	0.310

4.2.1 EIS

Plotting the resistance against the reciprocal of K_{config}, the gradient from Fig. 5a is A=$R_{RP,cell}$=0.0754 Ω and $R_{CA,cc}$=0.0235 Ω from the resistance intercept. Fig. 10 shows that the resistance of the μT-SOFC does indeed scale with the average resistance path with current collectors placed at the locations described in Fig. 2. The value of K_{config} used for positions A2 and A4 is 8/5. The resistances and the fitted resistances may be found in Table 3 for the EIS data.

4.2.2 Current-voltage data

Calculating the resistance from the gradient of the i-V curve, and restricting the data to the range of 0.5 to 0.7 V, the gradients are obtained, and the resistance of the cell is calculated. Plotting the resistance against the reciprocal of K_{config}, the gradient from Fig. 5b is A=$R_{RP,cell}$=0.0365 Ω and $R_{CA,cc}$=0.0775 Ω from the resistance intercept. The resistances and the fitted resistances may be found in Table 4 for the i-V data.

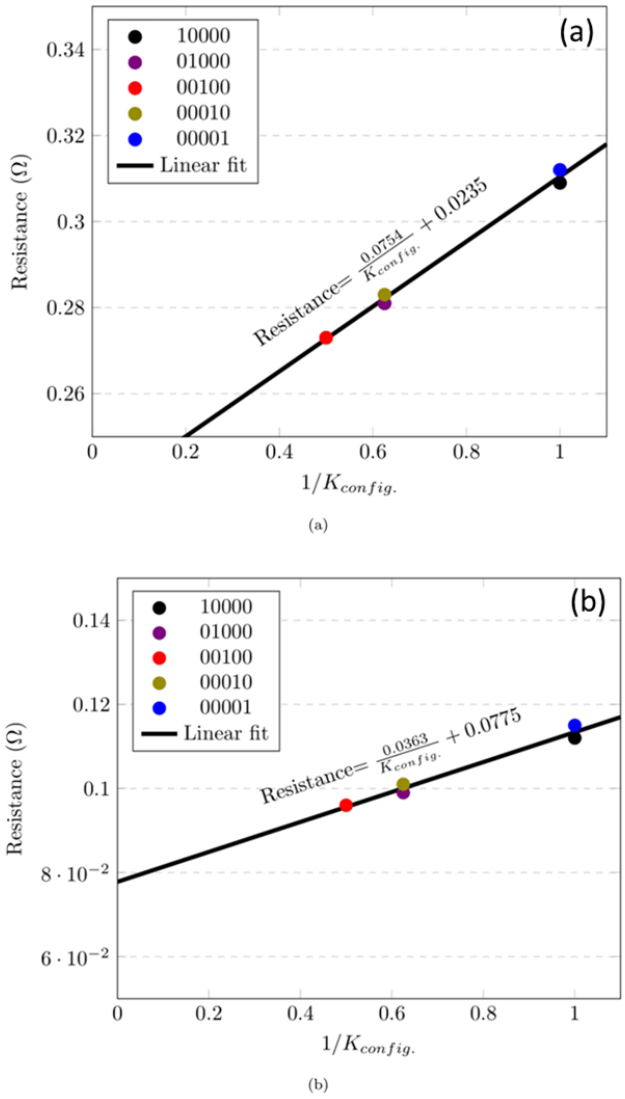

Figure 5: (a) Resistance of the different configurations plotted against the reciprocal of $K_{config.}$ using EIS data, (b) resistance of the different configurations plotted against the reciprocal of $K_{config.}$ using i-V curve data.

Table 4: Cell resistance obtained from i-V data and the fitted model resistance.

Configuration	Current collector position	$R_{ohmic}+R_{cell}$ (Ω) [i-V data]	Resistance path (Ω) [i-V parameters]
10000	**A1**	0.112	0.114
01000	**A2**	0.099	0.100
00100	**A3**	0.096	0.096
00010	**A4**	0.101	0.100
00001	**A5**	0.115	0.114

4.2.3 Comparison of EIS and IV parameters

In the three-current collector cases, the resistances were similar between the EIS and i-V case. For this particular five-current collector case, the resistances determined by i-V curve data are substantially less and the EIS-determined parameters are therefore larger. $R_{RP,cell}$ is approximately 2.17 times larger for the EIS case than with the i-V curve method, while $R_{CA,cc}$ values are 3 times larger for the EIS than the i-V curve method.

4.2.4 Average number of current collectors

As demonstrated in both the three- and five-current collector cases using a single current collector terminal, the position of the terminal impacts the effective resistance. Averaging over all the permutations of one, two, three, four and five current collector configurations, the experimental and theoretical results are shown in Fig. 6 (SM §3.5.2 for table of the K_{config} values). Using the EIS data, we find $A=R_{RP,cell}=0.0754$ Ω and $R_{CA,cc}=0.0235$ Ω, $V_0=0.95$ V, for $V=0.7$ V or 0.5 V, depending on the applied potential.

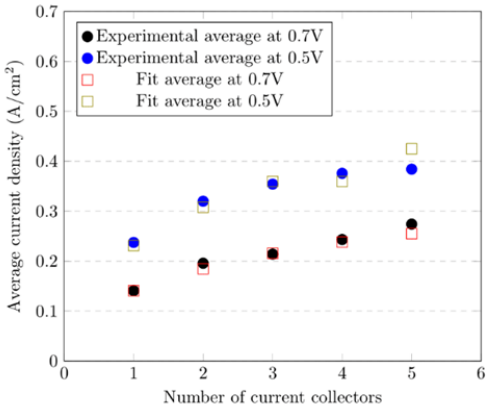

Figure 6: Empirical and numerical average current for singly connected 1 to 5 current collector nodes.

The 0.7 V data obtained from single current collectors describes the experimental data well and has the correct trend. It is interesting to note that the 0.7 V data slightly underestimates the 5-current collection case compared to the experimental data. The experimental uncertainty is larger than the theoretical discrepancy and is not considered significant. At 0.5 V it is interesting to note that in the 5-current collection case the fitted parameters for the single-current collection cases at 0.7 V performs remarkably well. It underestimates the experimentally found values, but the experimental uncertainty can be seen to explain this discrepancy. At 0.7 V the error for the single connection is ±0.020 $A.cm^{-2}$ and for the five-terminal connection is ±0.017 $A.cm^{-2}$. At 0.5 V the error for the single connection is ±0.030 $A.cm^{-2}$ and for the five terminal connections is ±0.069 $A.cm^{-2}$.

4.3 Asymmetry in resistances

There is evidence within the EIS and i-V curves that placing the current collector terminal immediately before the start of the active area produces a higher current than placing the current collector terminal immediately after the end of the active area. The influence accounts for a slight increase of 3% to the current density. However, this effect is consistent in all setups. There are two possible reasons for this, the resistance path of the current collectors are different, or the decrease in fuel partial pressure towards the end of the anode flow channel impacts the ability of the μT-SOFC to maintain a constant current density along the tube. Every effort has been put into ensuring the resistance path is the same for the current collectors, but temperature effects within the furnace may be at play here. The μT-SOFC conditions under investigation are with fuel in excess so that mass transport limitations would be avoided. The fixed flow rate but varied active area gave rise to two different ranges of fuel utilisation for each 3 terminal setup and 5 terminal setup at 0.7 V and another at 0.5 V. For the 3-terminal setup at 0.7 V, fuel utilisation was between 23 and 65% and at 0.5 V was between 51% and 64%. For the 5-terminal setup, the fuel utilisation at 0.7 V was 7% for the single terminal setup and 12% for the five terminal setup, rising to 11% and 18% at 0.5 V, respectively. The low fuel utilisation values ensure no change in

current output as a result of starvation and mitigate any losses that may occur from fuel leakages along the cell. The relatively high flow rates also help to smooth thermal gradients along the cell.

4.4 Optimisation and essential design considerations

Having developed a model capable of predicting the current measured by different configurations of ring-shaped current collection terminals, the model will be used in this section to determine optimal design. This section will consider the optimisation initially for the positioning of a single current collector of infinitesimal size, then for the optimal placement of an arbitrary number of infinitesimal current collectors. Once the key infinitesimal results are obtained, these are extended to current collector terminals of finite size. Two key current collector terminal location strategies are identified.

4.4.1 Geometry

The geometry used throughout this section for single current collectors is given in Fig. 1d. The total length depicted reaches from the start of the active area to the end of the active area. The center of the current collector is denoted by x and is the distance from the start of the μT-SOFC active area.

4.4.2 Optimal placement of ring-shaped current collection terminal for a single terminal

In the case of a single terminal of infinitesimal thickness, the minimum resistance path predicts a minimum in the resistance of the μT-SOFC. The average path length is given by (SM §3.1.1):

$$\langle l \rangle = (x^2 - Lx + L^2/2)/L \tag{11}$$

where x is the position measured from the start of the active area. The minimum of Eqn. (11) occurs when $x^* = L/2$, where x^* is the optimal placement of the infinitesimally thin electrode current collection terminal along the flow path of a μT-SOFC cell, in our case a ring-shaped terminal.

4.4.3 Optimal placement of current collectors with *n* terminals

The optimal placement of current collectors with an arbitrary integer of, *n* terminals is to minimise the average path length. In the case of 2 current collectors, the active area is split into three segments. The distance division at optimal placement is one of length, *m*, from the start of the μT-SOFC active area to the first current collector location. One of length, 2*m*, between the two current collectors and another segment of length, *m*, from the second current collector to the end of the μT-SOFC active area. The optimal placement is then $x_1^*=L/4$ and $x_2^*=3L/4$ for the first and second current collectors, respectively. The general case may be found in Table 5 and provide the optimal placement for *n* current collector terminals (SM §3.3).

4.4.4 Optimal size of current collector terminals

To allow for a real-world current collector terminal, the active area will be reduced due to part of the electrode being covered by the terminal; this again will reduce the current produced to some degree. However, the path length is also reduced. What is the optimal location and thickness of the current collector terminal? For a single current collector, ignoring the resistance $R_{RP,cc}$, the current will be given by (SM §3.1.7):

$$I=(V_0-V)r/R_{cell}((x-w/2)/(R_{cell}+r(x-w/2))+ (L-x-w/2)/(R_{cell}+r(L-x-w/2))) \quad (12)$$

the optimal placement from the critical points of Eqn. (12) is $x^*=L/2$ and $w^*=0$, where w^* is the optimal width of the current collector. The optimal width for a current collector is infinitesimal. However, the current collector must have finite size; that size being as small as possible.

4.4.5 Optimal locations vs sub-optimal locations

The optimal locations have been considered in Section 4.4.4 for *n* current collector terminals. However, since the current collector size is finite rather than infinitesimal, it is worth considering particular sub-optimal locations. The sub-optimal locations are also provided in Table 5.

Table 5: Locations of the center of current collector terminals for the two different current collector strategies.

n	Optimal locations	Sub-optimal locations
1	*L*/2	-*w*/2 or *L*+*w*/2
2	*L*/4, 3*L*/4	-*w*/2, *L*+*w*/2
3	*L*/6, *L*/2, 5*L*/6	-*w*/2, *L*/2, *L*+*w*/2
4	*L*/8, 3*L*/8, 5*L*/8, 7*L*/8	-*w*/2, *L*/3-*w*/6, 2*L*/3+*w*/6, *L*+*w*/2
5	*L*/10, 3*L*/10, *L*/2, 7*L*/10, 9*L*/10	-*w*/2, (*L*-*w*)/4, *L*/2, (3*L*+*w*)/4, *L*+*w*/2
n	L/(2n), (L+2L)/(2n), (L+4L)/(2n), …, (2nL-L)/(2n)	-w/2, (L-(n-2)w)/(n-1)+w/2, 2(L-(n-2)w)/(n-1)+3w/2, …, L+w/2

4.4.6 Optimal number of current collection terminals

The total length required for the optimal locations is *L*. For the sub-optimal locations, the total length is *L*+*w* if *n*=1 otherwise it is *L*+2*w*. The current density of different configurations can then be compared provided the appropriate total length is used. To identify the number of current collection terminals, the total resistance of the μT-SOFC can be multiplied by the total length and the minimum length specific resistance taken. The total resistance equations can be found in Table 6 for the optimal locations and Table 7 for the sub-optimal locations.

Table 6: Effective resistance for the optimal locations.

n	Total resistance- $R_{RP,cc}$
1	$R_{RP,cell}(R_{RP,cell}+r(L-w)/2)/(r(L-w))$
2	$R_{RP,cell}(R_{RP,cell}+r(L/2-w)/2)/(r(L-2w))$
3	$R_{RP,cell}(R_{RP,cell}+r(L/3-w)/2)/(r(L-3w))$
4	$R_{RP,cell}(R_{RP,cell}+r(L/4-w)/2)/(r(L-4w))$
n	$R_{RP,cell}(R_{RP,cell}+r(L/n-w)/2)/(r(L-nw))$

Table 7: Effective resistance for the sub-optimal locations.

n	Total resistance- $R_{RP,cc}$
1	$R_{RP,cell}(R_{RP,cell}+rL)/(rL)$
2	$R_{RP,cell}(R_{RP,cell}+rL/2)/(rL)$
3	$R_{RP,cell}(R_{RP,cell}+r(L-w)/4)/(r(L-w))$
4	$R_{RP,cell}(R_{RP,cell}+r(L-2w)/6)/(r(L-2w))$
n	$R_{RP,cell}(R_{RP,cell}+r(L-[n-2]w)/(2(n-1))/(r(L-[n-2]w))$

4.4.7 Number of terminals for a given length

This section provides an example of how Section 4.4.6 can be implemented to determine the optimal number of terminals for a given length. This is

defined in the introduction as the optimal strategy for a given definition of the current density (SM §3.3), but in this section is presented as minimising the ASR, an equivalent representation. The ASR is defined as the resistance multiplied by the total area. The total area is the total length multiplied by πd, the circumference of the μT-SOFC.

4.4.8 Optimal Locations

For a finite width current collector at the optimal locations there is a minimum in the resistance multiplied by the total length, this minimum is given for a length of:

$$L^{*}=n(w+\sqrt{(2wR_{RP,cell}/r)}) \quad (13)$$

and at this length the resistance is (SM §3.3):

$$R_{SOFC,min,O}=R_{RP,cell}(1+R_{RP,cell}/(rw+\sqrt{(2rwR_{RP,cell})})), \quad (14)$$

Eqn. (14) demonstrates that the resistance times the length corresponding to the optimal length is independent of *n*, as such a suitable choice of current collection strategy can maintain a high current density even for exceptionally long μT-SOFCs. Table 8 lists the length range for selection of number of terminals when using the optimal locations strategy.

Table 8: Resistance for the optimal locations (eqn 14).

N° of terminals	***Length range***
1	$w<L\leq 3w/2+\sqrt{w}\sqrt{(16R_{RP,cell}/r+w)}/2$
2	$3w/2+\sqrt{w}\sqrt{(16R_{RP,cell}/r+w)}/2\leq L \leq 5w/2+\sqrt{w}\sqrt{(48R_{RP,cell}/r+w)}/2$
3	$5w/2+\sqrt{w}\sqrt{(48R_{RP,cell}/r+w)}/2\leq L \leq 7w/2+\sqrt{w}\sqrt{(96R_{RP,cell}/r+w)}/2$
N	$(2n-1)w/2+\sqrt{w}\sqrt{(8n(n-1)R_{RP,cell}/r+w)}/2\leq L \leq (2n+1)w/2+\sqrt{w}\sqrt{(8n(n+1)R_{RP,cell}/r+w)}/2$

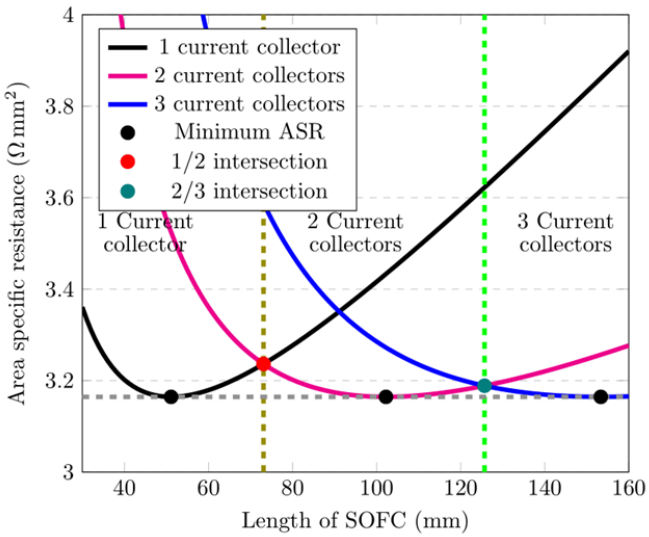

Figure 7: Area specific resistance (ASR) for a μT-SOFC using the optimal locations strategy: the black line represents a single current collector, magenta line represents two current collectors and the blue line represents 3 current collectors. The black filled circles are the optimal length for a single current collector, two current collectors and three current collectors. The transitions between the optimal number of current collectors is given by the red filled circle for the transition from 1 current collector to 2 and the filled cyan circle for the transition from 2 to 3. Parameters for this case are, $R_{RP,cell}$=0.0771 Ω, r=0.66356 Ω /m and w=8 mm.

Fig. 7 shows the ASR plot for one current collector (black line) with the current collector placed in the middle of the active region of the SOFC. The width of the current collector is 8 mm. As shown in Fig. 7, an ASR minimum is reached when the length of the active region is 51.12 mm obtained from Eqn. (13) (with n=1), the current collector's location is from 21.56 mm to 29.56 mm, and the centre is 25.56 mm as given by Table 5 (optimal locations, n=1, centre at L/2). The ASR increases in the single current collector case for lengths of the active region larger than 51.12 mm. When increasing the active region's length, the two current collector case (magenta line) eventually overtakes the ASR for a single current collector. The two ASRs are equal when the length of the SOFC is 73.11 mm. At equality, the 1/2 intersection, the red circle, corresponds to the two situations:

Single current collector (L=73.11 mm): The current collector's location is from 32.55 mm to 40.55 mm, with the centre placed at 36.55 mm [Table 5 (optimal locations, n=1, centre at L/2)].

Two current collectors (L=73.11 mm): The first current collector's location is from 14.28 mm to 22.28 mm, with the centre placed at 18.28 mm [Table 5 (optimal locations, n=2, centre at L/4)]. The second current collector site is from 50.83 mm to 58.83 mm, with the centre placed at 54.83 mm [Table 5 (optimal locations, n=2, centre at 3L/4)].

As with the single current collector case, the two current collectors case has a minimum of the ASR when the active region has a length of 102.23 mm obtained from Eqn. (13) (with n=2), the first current collector is located at 21.56 mm to 29.56 mm with the centre placed at 25.56 mm [Table 5 (optimal locations, n=2, centre at L/4)]. The second current collector is located at 72.68 mm to 80.68 mm, with the centre placed at 76.68 mm [Table 5 (optimal locations, n=2, centre at 3L/4)]. For lengths of the active region longer than 102.23 mm, the ASR increases in the two current collector case. For a length of 125.69 mm the ASR in the two current collector case is equal to the three current collector case and is represented by the 2/3 intersection, the cyan circle, this corresponds to the two situations:

Two current collectors (L=125.69 mm): The first current collector's location is 27.42 mm to 35.42 mm with the centre at 31.42 mm [Table 5 (optimal locations, n=2, centre at L/4)]. The second current collector site is 90.27 mm to 98.27 mm, with the centre located at 94.27 mm [Table 5 (optimal locations, n=2, centre at 3L/4)].

Three current collectors (L=125.69 mm): The first current collector's location is 16.95 mm to 24.95 mm with the centre at 20.95 mm [Table 5 (optimal locations, n=3, centre at L/6)]. The second current collector location is 58.85 mm to 66.85 mm with the centre located at 62.85 mm [Table 5 (optimal locations, n=3, centre at L/2)]. The third current collector site is 100.74 mm to 108.74 mm with the centre located at 104.74 mm [Table 5 (optimal locations, n=3, centre at 5L/6)].

Three current collectors have the minimum ASR at a length of 153.35 mm. The first current collector location is 21.56 mm to 29.56 mm with the centre at 25.56 mm [Table 5 (optimal locations, n=3, centre at L/6)]. The second current collector site is 72.68 mm to 80.68 mm with the centre located at 76.68 mm [Table 5 (optimal locations, n=3, centre at L/2)]. The third current collector site is 123.79 mm to 131.79 mm with the centre located at 127.79 mm [Table 5 (optimal locations, n=3, centre at 5L/6)].

4.4.9 Sub-optimal locations

Similarly, for the sub-optimal locations case a minimum resistance occurs for a total length (SM §3.4) of:

$$L^*=nw+\sqrt{}(2n(n\text{-}1)wR_{RP,\text{cell}}/r) \quad (15)$$

However, if n=1 the optimal total length is instead given by:

$$L^*=w+\sqrt{}(wR_{\text{RP,cell}}/r). \quad (16)$$

In the case of n=1 the minimum μT-SOFC resistance from the sub-optimal locations is given by:

$$R_{\text{SOFC,min,SO}}=R_{\text{RP,cell}}(1+\sqrt{}(R_{\text{RP,cell}}/(rw))) \quad (17)$$

and for the general case $n\geq 2$:

$$R_{\text{SOFC,min,SO}}=R_{\text{RP,cell}}(1/(2(n\text{-}1))+\sqrt{}(R_{\text{RP,cell}}/(2n(n\text{-}1)rw))) \quad (18)$$

It is worth noting that the limit as $n\to\infty$ is $R_{\text{SOFC,min,SO}}=R_{\text{SOFC,min,O}}$. The sub-optimal locations strategy always underperforms compared to the equivalent optimal locations strategy for any finite number of current collectors. Generally, the sub-optimal strategy is more easily incorporated into current design strategies than the optimal strategy. Furthermore, it is interesting to note that if the total length minus the current collection width, i.e. the active area length is used to perform the optimization the sub-optimal locations strategy outperforms the optimal locations strategy. In this case the current collectors are essentially free and so an infinite number of them performs best, but this case is not of particular interest unless the cost of the active area is very significant (SM §3.3 and 3.4).

5. Conclusion

Two models for optimising the current collection terminal locations in a μT-SOFC were developed, one based on the circuit analysis and the other based on resistance paths. The circuit analysis approach followed a similar approach to Suzuki et al. An exact

analytical representation for the circuit analysis was determined for the first time. A second model was developed based on a resistance path approach and it was found that the two models were equivalent. Since the resistance path model was built from a continuum assumption it was easier to optimise the model. Both models were validated by comparing to electrochemical experiments and typical fits to experimental data allowed for R^2 values above 90 %.

As such, the resistance path approach was optimised and an optimal strategy for current collection positioning was identified. An alternative strategy was also considered and found to perform worse than the optimal strategy but was easier to incorporate into current designs. Finally, the current collecting strategy allowed for μT-SOFCs to maintain efficient current generation even for exceedingly long μT-SOFCs.

Acknowledgement

This work was supported by the Centre for Doctoral Training (CDT) in Fuel Cells and their Fuels, which is part-funded by the EPSRC under contract EP/L015749/1.

References

[1] R. O'Hayre, S.-W. Cha, W. Celella, F.B. Prinz, Fuel Cell Fundamentals, Second, John Wiley & Sons, New York, 2009.

[2] R. Payne, J. Love, M. Kah, Generating Electricity at 60% Electrical Efficiency from 1 - 2 kWe SOFC Products, ECS Trans. 25 (2019) 231–239.doi:10.1149/1.3205530.

[3] M.M. Mench, Fuel Cell Engines, John Wiley & Sons, 2008.

[4] K. Kendall, M. Kendall, Index, in: High-Temperature Solid Oxide Fuel Cells 21st Century, Elsevier, 2016: pp. 497–508.doi:10.1016/B978-0-12-410453-2.09990-5.

[5] I.P. Kilbride, Preparation and properties of small diameter tubular solid oxide fuel cells for rapid start-up, J. Power Sources. 61 (1996) 167–171.doi:10.1016/S0378-7753(96)02362-2.

[6] K.S. Howe, A.R. Hanifi, K. Kendall, M. Zazulak, T.H. Etsell, P. Sarkar, Performance of microtubular SOFCs with infiltrated electrodes under thermal cycling, Int. J. Hydrogen Energy. 38 (2013) 1058–1067.doi:10.1016/j.ijhydene.2012.10.098.

[7] K.S. Howe, G.J. Thompson, K. Kendall, Micro-tubular solid oxide fuel cells and stacks, J. Power Sources. 196 (2011) 1677–1686.doi:10.1016/j.jpowsour.2010.09.043.

[8] K. Kendall, M. Kendall, K. Kendall, Portable early market SOFCs, in: High-Temperature Solid Oxide Fuel Cells 21st Century, Elsevier, 2016: pp. 329–356.doi:10.1016/B978-0-12-410453-2.00010-5.

[9] K. Kendall, M. Kendall, K. Kendall, Introduction to SOFCs, in: High-Temperature Solid Oxide Fuel Cells 21st Century, Elsevier, 2016: pp. 1–24.doi:10.1016/B978-0-12-410453-2.00001-4.

[10] M.A. Hirofumi Sumi, Hiroyuki Shimada, Toshiaki Yamaguchi, Yoshinobu Fujishiro, Development of portable solid oxide fuel cell system driven by hydrocarbon and alcohol fuels, in: 42nd Int. Conf. Adv. Ceram. Compos. Ceram. Eng. Sci., 2019: pp. 159–163.doi:doi:10.1002/9781119543343.ch15.

[11] O. Aydin, H. Nakajima, T. Kitahara, Current and temperature distributions in-situ acquired by electrode-segmentation along a microtubular solid oxide fuel cell operating with syngas, J. Power Sources. 293 (2015) 1053–1061.doi:10.1016/j.jpowsour.2015.06.024.

[12] S.M. Jamil, M.H.D. Othman, M.A. Rahman, J. Jaafar, A.F. Ismail, K. Li, Recent fabrication techniques for micro-tubular solid oxide fuel cell support: A review, J. Eur. Ceram. Soc. 35 (2015) 1–22.doi:10.1016/j.jeurceramsoc.2014.08.034.

[13] H. Sumi, T. Yamaguchi, K. Hamamoto, T. Suzuki, Y. Fujishiro, Experimental and Simulated Evaluations of Current Collection Losses in Anode-Supported Microtubular Solid Oxide Fuel Cells, J. Electrochem. Soc. 160 (2013) 1232–1236.doi:10.1149/2.031311jes.

[14] S.L. Zhang, C.X. Li, S. Liu, C.J. Li, G.J. Yang, P.J. He, L.L. Yun, B. Song, Y.X. Xie, Thermally Sprayed Large Tubular Solid Oxide Fuel Cells and Its Stack: Geometry Optimization, Preparation, and Performance, J. Therm. Spray Technol. 26 (2017) 441–455.doi:10.1007/s11666-016-0506-5.

[15] Y. Bai, C. Wang, C. Jin, J. Liu, Anode Current Collecting Efficiency of Tubular Anode-supported Solid Oxide Fuel Cells, Fuel Cells. 11 (2011) 465–468.doi:10.1002/fuce.201000053.

[16] A. Meadowcroft, K. Howe, A. Dhir, R. Steinberger-Wilckens, Connection Optimisation for Micro-Tubular Solid Oxide Fuel Cells (A1507), in: 11th Eur. SOFC SOE Forum, Lucerne Switzerland, 2014.

[17] T. Suzuki, T. Yamaguchi, Y. Fujishiro, M. Awano, Current collecting efficiency of micro tubular SOFCs, J. Power Sources. 163 (2007) 737–742.doi:10.1016/j.jpowsour.2006.09.071.

[18] T. Suzuki, Y. Funahashi, T. Yamaguchi, Anode-supported micro tubular SOFCs for advanced ceramic reactor system, J. Power Sources. 171 (2007) 92–95.doi:10.1016/j.jpowsour.2007.01.003.

[19] O. Hodjati-Pugh, A. Dhir, R. Steinberger-Wilckens, Internal Current Collection in Microtubular SOFCs : Minimisation of Contact Resistance via Brazing and Plating, ECS Trans. 91 (2019) 553–548.doi:doi.org/10.1149/09101.0533ecst.

[20] Aremco, Aremco Ceramabond ™ 552 High Temperature Ceramic Adhesive/Paste, Alumina Filled, (2019). http://www.matweb.com/search/datasheet.aspx?matguid=e6b75c1c0a4f46ec8a4f3bff3bc828e3&ckck=1 (accessed September 1, 2020).

[21] SCHOTT AG, SCHOTT Glass and Glass-Ceramic Sealants for Technical Ceramics in High-Temperature Applications SCHOTT Glass and Glass-Ceramic Sealants for Technical Ceramics in High-Temperature Applications, 530 (2019). https://www.schott.com/d/epackaging/bb967de5-a550-4e8f-85c5-b337021f2e11/1.4/schott-cerajoin-sealing-glass-ceramic-sealant-for-high-temperatures_eng.pdf (accessed March 24, 2020).